CEAS-GNC-2022-073

CEAS EuroGNC 2022
"Conference on Guidance, Navigation and Control"
3-5 May 2022 @ Technische Universität Berlin, Germany

Terminal Phase Nonlinear Attitude Autopilot Design For Dual-Spin Guided Projectiles

Sofiane Pineau PhD student, University of Lorraine, CRAN-UMR-CNRS-7039, France. & French-German Research Institute of Saint-Louis, Department of Guidance, Navigation and Control, 68300, Saint-Louis, France. sofiane.pineau@isl.eu

Spilios Theodoulis Flight Dynamics and Control Research Scientist, French-German Research Institute of Saint-Louis, Department of Guidance, Navigation and Control, 68300, Saint-Louis, France. spilios.theodoulis@isl.eu

Michel Zasadzinski Professor, University of Lorraine, CRAN-UMR-CNRS-7039, France. michel.zasadzinski@univ-lorraine.fr

Mohamed Boutayeb Professor, University of Lorraine, CRAN-UMR-CNRS-7039, France. mohamed.boutayeb@univ-lorraine.fr

ABSTRACT

This article proposes a straightforward methodology applied to the design of a nonlinear attitude autopilot for a 155 mm spin-stabilized projectile equipped with a roll-decoupled course-correction fuze. The primary purpose of the autopilot is to control the projectile pitch and yaw angles during the terminal phase of its trajectory in order to handle impact angles arrival. The nonlinear attitude flight dynamics model is first summarized along with all necessary subsystem models such as aerodynamic moments, control allocation and actuators. The Incremental Nonlinear Dynamic Inversion (INDI) was used to successfully linearize the roll and lateral dynamics. Linear robust $\mathscr{H}_\infty$ controllers were subsequently designed in an inner/outer loop configuration to ensure proper reference angle tracking of the projectile dynamics. Practical implementation constraints such as finite computational sampling time and potential on-board delays were integrated into the design process via a standard Modified Continuous Design technique and the impact of low sampling frequency on INDI decoupling capacity was investigated. Full trajectory nonlinear simulation results show a successful implementation of the INDI control laws in terms of tracking performance and axis decoupling.

Keywords: dual-spin projectiles, Incremental Nonlinear Dynamic Inversion, autopilot design, flight dynamics

1 Introduction

Standard spin-stabilized 155 mm projectiles, widely used in artillery, suffer from a relatively high dispersion around a target due to uncertainties on firing conditions or wind disturbances. This results to several ammunition launches in order to successfully engage the objective. Multiple firings though imply a higher cost for the operation and potentially increased collateral damages as well as a higher risk for the military personnel since the mission time increases. To deal with this lack of precision, a low cost and innovative solution is to equip existing unguided projectiles with a decoupled guidance fuze which embeds up to four aerodynamic control surfaces, sensors, actuators and GNC software. The

guided projectile is hence expected to potentially reach metric precision around the target.

Many flight control laws designed for spin-stabilized projectiles that can be found in the literature employ gain-scheduling techniques based on the local linearization of the projectile dynamics around a given number of flight points [1–4]. This approach gives satisfactory results while allowing for the use of well-known robust control theory tools. However, due to its nature gain-scheduling has two main drawbacks: first, it can be time-consuming since the control engineer most often needs local linear models of the studied dynamics computed about a significant number of operating points for the autopilot design to be successful. Secondly, the obtained nonlinear controller resulting from the interpolation of linear controllers can only guarantee performance and stability of the closed-loop system in the vicinity of the aforementioned flight points [5].

This fact motivates the need for a more generic methodology dedicated to fast design using nonlinear flight control techniques such as sliding mode control [6], backstepping [7, 8], or Nonlinear Dynamic Inversion (NDI)[9–12] and its sensor-based incremental form (INDI) [13–16]. The latter technique requires the tuning of only a single linear controller to cover the whole flight envelope and promises good performance and robustness against model mismatch. More precisely, the INDI technique is supposed to be more robust than classical NDI since by basing its inversion on the actual sensors, actuator data and acceleration estimation, it is less dependent on the model parameters [14] especially if these subsystems are sufficiently accurate. Another advantage of inversion-based nonlinear techniques, is that by dynamically inverting the plant, the system acts like a chain of integrators for all flight envelope which is subsequently quite easy to control by a single linear controller.

In the case of a spin-stabilized projectile there is an important amount of coupling between the lateral axes due to the projectile spin, as well as increased uncertainty on the various aerodynamic coefficients. INDI is supposed to offer a perfect decoupling between axes, however results presented in this paper show the degrading effect of a low sampling frequency on INDI inversion. That's why, multivariable linear controllers in the outer loop configuration are a relevant solution to deal with INDI imperfect decoupling. To this end, a mixed-sensitivity layout [17] and multi-objective design tools were employed in a systematic manner to handle the various time and frequency control constraints.

In this article a practical and straightforward nonlinear autopilot design methodology is proposed and applied to the design of a terminal phase angle autopilot which is challenging and unconventional for spin-stabilized projectiles but relevant in operational scenarios where full control of pitch and yaw angles is needed. This paper is organized as follows: Section 2 presents the projectile attitude nonlinear model, Section 3 is dedicated to flight control design where the methodology applied to the design of a terminal phase nonlinear autopilot is discussed and every design step is detailed. The last part shows nonlinear full trajectory simulations according to two proposed scenarios.

2 Nonlinear Attitude Flight Dynamics Model

The studied spin-stabilized guided projectile is illustrated by Fig. 1. The projectile has two roll-decoupled parts: the main body called the aft part which rotates at a high spin rate, stabilizing the projectile and the fuze part, controlling the projectile trajectory using two pairs of canards associated with necessary hardware and GNC softwares. This section presents and summarizes the nonlinear attitude flight dynamics model followed by the external moments expressions and the actuators model.

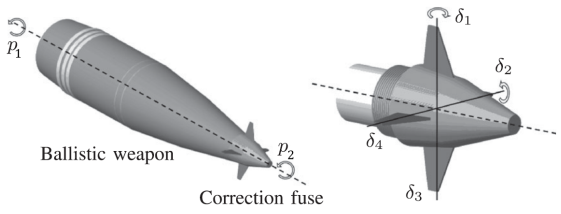

Fig. 1 Decoupled Fuze Guided Projectile

2.1 Frames and Coordinate Systems

The equations of motion are expressed in mostly two coordinate systems which are linked to the parts of the projectile: $]^{B_1}$ for the aft part and $]^{B_2}$ for the fuze part. More precisely a $]^{B'_1}$ coordinate system related to a non-rolling frame B'_1 is used, it undergoes the same movements as the aft part except for the roll motion which is fixed. The coordinate system $]^{B'_1}$ is preferred because the roll angle of the aft part and its derivatives are always zero, this coordinate system is therefore more adapted to high spinning bodies compared to a classical rolling frame which needs a small integration step resulting in longer and less accurate simulations.

2.2 Attitude Dynamics

The attitude dynamic equations describe the main body and the fuze rotation around their respective centers of gravity. The aft part attitude dynamics is given by [18]:

$$\left[\tilde{I}_B^{B_{1,2}}\right]^{B'_1}\left[\frac{\mathrm{d}\omega^{B_1E}}{\mathrm{d}t}\right]^{B'_1}+\left[\Omega^{B'_1E}\right]^{B'_1}\left[\tilde{I}_B^{B_{1,2}}\right]^{B'_1}[\omega^{B_1E}]^{B'_1}=[m_{B_1}]^{B'_1} \tag{1}$$

where $\left[\tilde{I}_B^{B_{1,2}}\right]^{B'_1}$ is the effective moment of inertia (MoI) of the projectile aft part, $\left[\omega^{B_1E}\right]^{B'_1}$ is the angular velocity vector of the aft part, $\left[\Omega^{B'_1E}\right]^{B'_1}$ the skew-symmetric matrix of the non-rolling frame with respect to the earth and $[m_{B_1}]^{B'_1}=[L_1 \quad M \quad N]^\top$ is the moment vector applied on the aft part of the projectile. The MoI $\left[\tilde{I}_B^{B_{1,2}}\right]^{B'_1}$ is diagonal due to the projectile tetragonal symmetry and is computed using clustered body theory [18]:

$$\left[I_B^{B_{1,2}}\right]^{B'_1} = \left[I_{B_1}^{B_1}\right]^{B'_1}+m^{B1}\left(\left[\overline{S}_{B_1B}\right]^{B'_1}[S_{B_1B}]^{B'_1}\right)+\left[\overline{T}\right]^{B_2B'_1}\left[I_{B_2}^{B_2}\right]^{B_2}+m^{B2}\left(\left[\overline{S}_{B_2B}\right]^{B'_1}[S_{B_2B}]^{B'_1}\right) \tag{2a}$$

$$\left[\tilde{I}_B^{B_{1,2}}\right]^{B'_1} = \left[I_B^{B_{1,2}}\right]^{B'_1}-\left[\overline{T}\right]^{B_2B'_1}\left[I_{B_2}^{B_2}\right]^{B_2} \tag{2b}$$

with $\left[I_B^{B12}\right]^{B'_1}$ the projectile total MoI, $\left[I_{B_1}^{B_1}\right]^{B'_1}$ the MoI related to the aft part and $\left[I_{B_2}^{B_2}\right]^{B_2}$ the MoI related to the fuze part. B_1, B_2 are respectively the center of mass of the aft and fuze part and B is the projectile real center of mass. A transformation matrix $[T]^{B_2B'_1}$ is used, which depends of fuze roll angle . Finally, $[S_{B1B}]^{B'_1}$ and $[S_{B2B}]^{B'_1}$ are the skew-symmetric matrix of the displacement vectors $s_{B_1B}=[x_{B_1B} \quad 0 \quad 0]^\top$ and $s_{B_2B}=[x_{B_2B} \quad 0 \quad 0]^\top$.

$$\left[I_{B_2}^{B_2}\{1,1\}\right]^{B_2}\left[\frac{\mathrm{d}p_2^{B_2E}}{\mathrm{d}t}\right]^{B_2}=[m_{B_2}\{1,1\}]^{B_2} \tag{3}$$

The full attitude dynamics equations are obtained by computing the four rotation degrees of freedom made of the body roll, pitch and yaw motions plus the roll motion of the fuze part of the projectile given by Eq. (3), with $[m_{B_2}]^{B_2}=[L_2 \quad M \quad N]^\top$ the moment vector applied on the fuze part of the projectile. From the tensor expression of Eq. (1) and Eq. (3) the following matrix equation is obtained.

$$\begin{bmatrix}\dot{p}_2\\ \dot{p}_1\\ \dot{q}\\ \dot{r}\end{bmatrix}=\begin{bmatrix}I_{x_2}^{-1}&0&0&0\\ 0&\tilde{I}_{x_1}^{-1}&0&0\\ 0&0&\tilde{I}_t{}^{-1}&0\\ 0&0&0&\tilde{I}_t{}^{-1}\end{bmatrix}\left(\begin{bmatrix}0&0&0&0\\ 0&0&r&-q\\ 0&-r&0&-r\tan\theta\\ 0&q&r\tan\theta&0\end{bmatrix}\begin{bmatrix}I_{x_2}&0&0&0\\ 0&\tilde{I}_{x_1}&0&0\\ 0&0&\tilde{I}_t&0\\ 0&0&0&\tilde{I}_t\end{bmatrix}\begin{bmatrix}p_2\\ p_1\\ q\\ r\end{bmatrix}+\begin{bmatrix}L_2\\ L_1\\ M\\ N\end{bmatrix}\right) \tag{4}$$

2.3 External Moments

The external moments applied on the projectile are composed of aerodynamic and mechanical actions. In addition to the drag and lift (P), the projectile is subjected to the Magnus effect (M) due to its high spin rate, and damping forces caused by air friction (D). Moreover, the fuze creates a control force and a moment (C) in function of canards deflection $[\delta_p \quad \delta_q \quad \delta_r]^\top$. More precisely, $[\delta_p \quad \delta_q \quad \delta_r]^\top$ are the roll, pitch and yaw control signals given by the autopilot. Section 2.4 gives a more detailed explanation about the relation between autopilot commands and each real canards deflection.

$$\left[m_B^{1,2}\right]^{B_{1'},2} = \left[m_B^{\mathrm{P}}\right]^{B_{1'},2} + \left[m_B^{\mathrm{M}}\right]^{B_{1'},2} + \left[m_B^{\mathrm{D}}\right]^{B_{1'},2} + \left[m_B^{\mathrm{C}}\right]^{B_{1'},2} \tag{5}$$

$$\begin{bmatrix} L_2 \\ L_1 \\ M \\ N \end{bmatrix} = \bar{q}Sd \left(\begin{bmatrix} 0 \\ 0 \\ C_{m_\alpha} \sin\alpha\cos\beta \\ -C_{m_\alpha} \sin\beta \end{bmatrix} + \frac{p_1 d}{2V} \begin{bmatrix} 0 \\ 0 \\ C_{n_{p\alpha}} \sin\beta \\ -C_{n_{p\alpha}} \sin\alpha\cos\beta \end{bmatrix} + \frac{d}{2V} \begin{bmatrix} 0 \\ C_{l_p} p_1 \\ C_{m_q} q \\ -C_{m_q} r \end{bmatrix} + \begin{bmatrix} C_{l_\delta}\delta_p \\ 0 \\ C_{m_\delta}(\delta_q + \alpha) \\ C_{m_\delta}(\delta_r - \beta) \end{bmatrix} \right) \tag{6}$$

where α, β are the angle of attack and the angle of sideslip respectively, obtained from the body velocity vector with respect to the air $\left[v_B^A\right]^{B_1'}$, S is the reference area of the projectile, d the caliber and $\bar{q}$ is the dynamic pressure defined as $\frac{1}{2}\rho V^2$ with $\rho(h)$ the altitude-dependent air density and V the airspeed. The moment aerodynamic coefficients $C_{m_\alpha}, C_{n_{p\alpha}}, C_{l_p}, C_{m_q}, C_{l_\delta}, C_{m_\delta}$ are obtained using computational fluid dynamics simulation and wind tunnel tests. Experimental data are then interpolated as a function of the total angle of attack α' and the Mach number $\mathscr{M} = \frac{V}{a(h)}$ where a is the speed of sound which is dependent of the altitude. An additional moment of friction $\left[m_B^F\right]^{B_{1'2}}$ can be added to the sum of moments as friction exist between the fuze and the aft part of the projectile, it increases the spin rate of the fuze and reduce the spin rate of the main body. The constants K_s, and K_v are the coefficient of static and viscous friction respectively and C_A is the axial force aerodynamic coefficient.

$$\left[m_B^F\right]^{B_{1'2}} = \bar{q}SdC_A \mathrm{sgn}\left(p_1 - p_2\right)\left(K_s + K_v\right)\left|p_1 - p_2\right| \begin{bmatrix} 1 \\ -1 \\ 0 \\ 0 \end{bmatrix} \tag{7}$$

2.4 Control Allocation and Actuator Model

The course correction fuze is composed by four aerodynamics control surfaces called canards, creating forces and moments on the projectile, allowing the control of the fuze roll and the projectile lateral motion by aerodynamic actions. A relation is made by the control allocation matrix $[T]^{VR}$ between the the virtual commands $[\delta_{\mathrm{v}}] = [\delta_p \quad \delta_q \quad \delta_r]^\top$ given by the autopilot and the real commands intended for each canards servo motors $[\delta_{\mathrm{r}}] = [\delta_1 \quad \delta_2 \quad \delta_3 \quad \delta_4]^\top$. Virtual commands are expressed in $]^{B_1'}$ coordinate system whereas the real commands are expressed in $]^{B_2}$ coordinate system. The full relation is obtained with Eq. (8) :

$$[\delta_{\mathrm{v}}]^{B_1'} = \left[\overline{T}\right]^{B_2 B_1'} [T]^{\mathrm{VR}} [\delta_{\mathrm{r}}]^{B_2} \tag{8}$$

$$[T]^{\mathrm{VR}} = \begin{bmatrix} -1/4 & 1/4 & 1/4 & -1/4 \\ 1/2 & 0 & 1/2 & 0 \\ 0 & 1/2 & 0 & 1/2 \end{bmatrix} \tag{9}$$

As INDI is sensitive to actuators speed and accuracy, implementing an INDI control law with a non perfect actuator model is relevant for evaluating performance of the autopilot in more realistic conditions. To this end, while sensors are supposed to be perfect, each canard is modeled by a second order transfer function, with $\omega_\delta = 375$ rad/s and $\xi_\delta = 0.707$:

$$G_\delta(s) = \frac{\omega_\delta^2}{s^2 + 2\xi_\delta\omega_\delta + \omega_\delta^2} \tag{10}$$

3 Flight Control Design

This section is dedicated to flight control design with discrete-time INDI for the control of the lateral angles of the projectile. First of all, after a general introduction on INDI, the relevance of INDI implementation on spin-stabilized projectiles is discussed, then the nonlinear design methodology proposed is explained. The independent control of pitch and yaw angles is achieved through several steps: the stabilization of the fuze roll angle, the projectile lateral channels rate decoupling and the control of pitch and yaw angles. In the remaining part of this article, a focus is given on lateral channels decoupling and pitch and yaw angles control since these two aspects are the core of the control problem and the main novelty of this paper. Therefore, the roll autopilot design is not detailed.

3.1 Incremental Nonlinear Dynamic Inversion

The dynamics of a spin-stabilized projectiles is strongly nonlinear and coupled so nonlinear inversion based techniques like NDI and INDI which presents good decoupling capacities are a legitimate approach to face the concerned control problem. Inversion-based autopilots are structured in an inner/outer loop configuration as presented in Fig. 2. While the inner loop inverts and linearizes the plant dynamics which then act ideally like a chain of integrators, the outer loop sets the desired closed-loop behavior with an external linear controller. NDI has a lot of successfully application in the aeronautics community [9–11] and is more easy and straightforward to design than "divide and conquer" techniques like gain-scheduling. However, its main drawback is its lack of robustness due to its high dependency to model accuracy. Actually, parametric uncertainties can strongly degrade NDI performance because nonlinearities are no longer canceled. This high dependency on good model knowledge can be an issue as the model of the presented dual-spin projectile is subject to some significant uncertainties for the aerodynamic coefficients.

Initially known as simplified NDI [19] then modified NDI [20], Incremental Nonlinear Dynamic Inversion is a reformulation of NDI based on time-scale separation between state dynamics and actuator dynamics (this assumption was discussed by [13]). INDI is known to be much less dependent on the model than NDI, more robust to parametric uncertainties and provides with a simpler control law. More precisely, only parameters related to control effectiveness are needed to compute the control signal. The lack of information concerning the rest of the model is compensated by the use of actuators position measurement and state derivative which for the last one, can either be measured or estimated by differentiation.

Finally, as INDI theory is based on time-scale separation between actuators and state dynamics the actuators need to be sufficiently fast. Accurate sensors are also necessary to provide reliable data for INDI inner loop computation. In the end, INDI was chosen for the design because of its quasi-independency of model knowledge and its simple and more generic implementation, more suitable for the design methodology proposed. INDI fundamentals equations in discrete time are recalled in the Appendix.

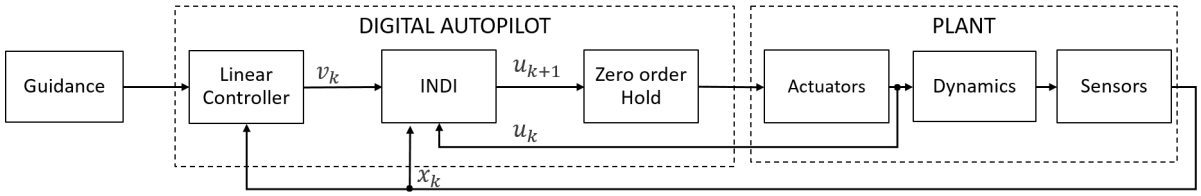

Fig. 2 INDI digital autopilot architecture

3.2 Design Methodology

The methodology used for the discrete-time nonlinear autopilot design is detailed in the following subsections, even if in this paper, INDI was used, the proposed approach can be adapted to other inversion based control laws. This methodology is intended to be straightforward and dedicated to generic and fast design of nonlinear autopilot.

3.2.1 Study of the Analytical Expression of the INDI Command

The first step of the design methodology is to compute the analytical expression of INDI command according to Eq. (11) applied to the studied dynamics. The inverse of control effectiveness matrix G is defined and its invertibility is verified for all flight envelope. A sampling period $T = \frac{1}{300}$ is used for digital implementation, which is half of the sensors sampling period. This ensure the autopilot has always the last measurements available for INDI computation.

$$\boldsymbol{u}[k+1] = \boldsymbol{u}[k] + G^{-1}\left(\boldsymbol{v}[k] - \frac{\boldsymbol{x}[k] - \boldsymbol{x}[k-1]}{T}\right) \tag{11}$$

3.2.2 Discrete-Time Inverted Model Identification

Once the expression of the control signal $\boldsymbol{u}[k+1]$ is expressed analytically, a nonlinear model of the studied dynamics for a single flight point is implemented in Simulink. The objective is to verify that the studied dynamics act like a chain of integrators with INDI inner loop and evaluate the effect of sampling frequency on the inversion. This leads to the identification of an equivalent continuous-time inverted model with sampling period dependency which catches the dynamics of INDI inner loop. The obtained linear model is used in the design model for the tuning of the external controller.

3.2.3 External Controller Design and Discretization

The performance of the autopilot depends to a large extent on the tuning of the external controller. Thanks to dynamic inversion, the system to be controlled is reduced to a chain of integrators. Even if a digital controller is desired, it is more convenient to tune the external controller in continuous time. To this end, standard Modified Continuous Design [21] is used. This technique consists of improving the continuous design by adding into the design model Zero Order Hold and computational delay transfer functions using Padé approximants, in this manner implementation constraints are taken into account resulting in a digital controller with better performance [21]. The gains are tuned following classical linear $\mathscr{H}_\infty$ robust control theory as the inverted dynamics model used for the tuning is linear, weighting filters values used for each design are available in appendix. The synthesized controller is then discretized using Tustin's bilinear transform (12). A performance comparison between unmodified and modified continuous design for a 100 Hz discretized controller is available in appendix.

$$z = e^{sT} \approx \frac{1 + sT/2}{1 - sT/2} \tag{12}$$

3.2.4 Nonlinear Autopilot Validation

The last step is the validation of the autopilot. First, frequency results of the synthesized controller are assessed in accordance to design requirements, in a second step, the external controller is tested with the INDI inner loop in a single flight point nonlinear model to verify performance in terms of tracking and decoupling. Finally the autopilot is implemented and validated for all trajectory in the full nonlinear parameter-varying simulator.

3.3 Roll Autopilot Design

As explained at the beginning of Section 3, the methodology proposed was first applied to the design of a roll autopilot used for the stabilization of the fuze roll angle. More precisely, the projectile aft part has a spin rate of 300 Hz which stabilize the body and due to this spin rate and the friction between the fuze and the main body the fuze spin rate increases resulting in a fast rotating fuze. The fuze roll angle needs to be stabilized to provide with a stable environment for the projectile lateral control. Fig. 3 shows a nonlinear simulation of the successful stabilization of the fuze roll angle. It should be noticed that the fuze spin rate is first reduced by putting all canards into saturation before launching the autopilot.

3.4 Lateral Channels Decoupling

In this part, the methodology presented is Section 3.2 is applied to the control and decoupling of the lateral rate dynamics. The fuze roll angle is considered already stabilized at $\phi_2 = 0$ deg.

3.4.1 Lateral Channels INDI Equations

The dynamic equations for the lateral channels are obtained from Eq. (4) and Eq. (6). $\begin{bmatrix}\delta_q & \delta_r\end{bmatrix}^\top$ are the control signal which will ensure the input/output linearization.

$$\begin{cases} \dot{q} = \frac{\tilde{I}_{x_1}}{\tilde{I}_t} p_1 r - r^2 \tan\theta + \frac{M}{\tilde{I}_t} \\ \dot{r} = \frac{\tilde{I}_{x_1}}{\tilde{I}_t} p_1 q - qr \tan\theta + \frac{N}{\tilde{I}_t} \end{cases} \tag{13}$$

Because of the symmetry of the projectile around the roll axis, the control effectiveness G matrix is diagonal as δ_q and δ_r are both multiplied by $\left(\frac{\bar{q}Sd}{\tilde{I}_t}\right) C_{m_\delta}$ and can be easily identified. With C_{m_δ} and $\bar{q}, S,$ and d always strictly positive, G is invertible for all flight envelope leading to the discrete-time INDI control signal equation for lateral channels (15) derived from Eq. (11).

$$G = \begin{bmatrix} \frac{\mathrm{d}\dot{q}}{\mathrm{d}\delta_q} & \frac{\mathrm{d}\dot{q}}{\mathrm{d}\delta_r} \\ \frac{\mathrm{d}\dot{r}}{\mathrm{d}\delta_q} & \frac{\mathrm{d}\dot{r}}{\mathrm{d}\delta_r} \end{bmatrix} = \begin{bmatrix} \left(\frac{\bar{q}Sd}{\tilde{I}_t}\right) C_{m_\delta} & 0 \\ 0 & \left(\frac{\bar{q}Sd}{\tilde{I}_t}\right) C_{m_\delta} \end{bmatrix} \tag{14}$$

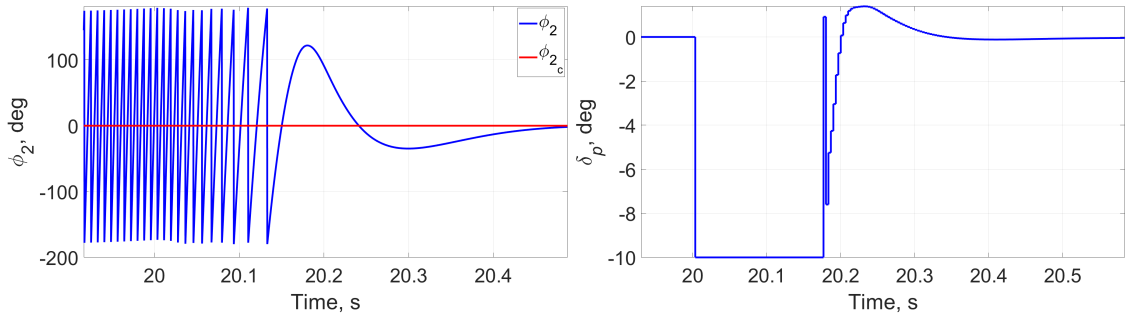

Fig. 3 INDI roll autopilot step response in nonlinear simulation

$$\begin{bmatrix}\delta_q[k+1]\\ \delta_r[k+1]\end{bmatrix} = \begin{bmatrix}\delta_q[k]\\ \delta_r[k]\end{bmatrix} + \begin{bmatrix}\frac{\tilde{I}_t}{\bar{q}SdC_{m_\delta}} & 0\\ 0 & \frac{\tilde{I}_t}{\bar{q}SdC_{m_\delta}}\end{bmatrix} \begin{bmatrix}v_q[k] - \frac{q[k]-q[k-1]}{T}\\ v_r[k] - \frac{r[k]-r[k-1]}{T}\end{bmatrix} \tag{15}$$

3.4.2 Discrete-Time Inverted Model

Dynamic equations (13) are implemented in a one flight point nonlinear model to first, verify the linearization of lateral channel dynamics by Eq. (15) and then identify the real INDI inner loop transfer function that will be used for the tuning of the external controller. Under ideal conditions (continuous time, no delays or measurement bias), INDI inner loop offers perfect decoupling between pitch and yaw channel:

$$\begin{bmatrix}q\\ r\end{bmatrix} = \begin{bmatrix}\frac{1}{s} & 0\\ 0 & \frac{1}{s}\end{bmatrix} \begin{bmatrix}q_c\\ r_c\end{bmatrix} \tag{16}$$

However with a finite sampling time, the anti diagonal terms are no longer zero and tend to be more important as sampling time increases which reveals the degrading effect of sampling frequency on INDI performance. Considering this phenomena, an estimation of the influence of sampling time on INDI decoupling capacity was conducted by evaluating the gains of the anti-diagonal terms compared to diagonal terms in Eq. (32). Frequencies from 100Hz to 2000Hz were studied with a 1Hz resolution resulting in Fig. 4. With a typical sampling frequency of 300 Hz, remaining coupling is not negligible and needs to be taken into account for the design. In order to fully decouple the lateral dynamics a full-order multivariable $\mathscr{H}_\infty$ controller was used. An analytical expression of the inverted model can not be easily identified, that's why a numerical estimation was used provided by Matlab/Simulink linearization tools subsequently converted in continuous time for the external controller tuning.

3.4.3 Full Order $\mathscr{H}_\infty$ Controller Tuning

The tuning of the controller in the made in continuous time using first and third order Pade approximant for ZOH and computational delay respectively in the design model.

$$G_{\text{ZOH}}(s) = \frac{1-sT/6}{1+sT/3} \tag{17a}$$

$$G_d(s) = \frac{1}{1+sT+(sT)^2/2+(sT)^3/6} \tag{17b}$$

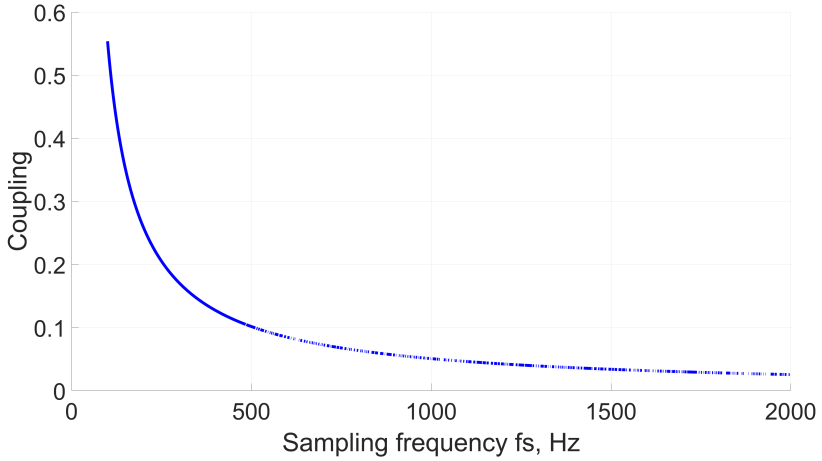

Fig. 4 Influence of the sampling frequency on INDI decoupling capacity for lateral channels

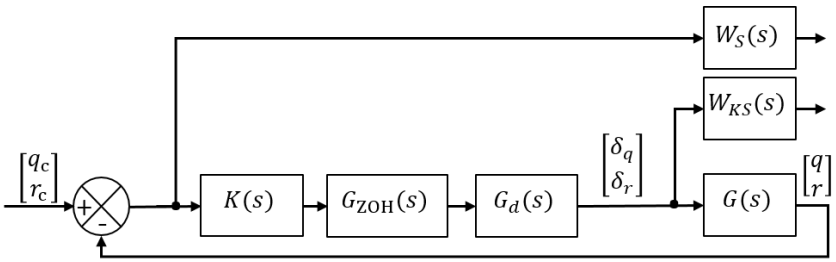

Fig. 5 Mixed-sensitivity design layout for lateral channels decoupling

Figure 9 shows the design layout employed, with $K(s)$ the tuned controller and $G(s)$ the lateral dynamics inverted model identified in Section 3.4.2. The actuators dynamics is not included in the design model as its effect on INDI is already taken into account in the numerical estimation of the inverted model. To guarantee good reference tracking with satisfactory disturbance rejection a mixed-sensitivity S/KS approach was used [17]. $W_S(s)$ and $W_{KS}(s)$ are the weighting filters used to shape in the frequency domain the transfer functions of the system according to the design specifications. $W_S(s)$ and $W_{KS}(s)$ were chosen according to Eq. (18) [17] as:

$$W(s) = \left(\frac{\frac{s}{M^{\frac{1}{k}}} + \omega_b}{s + \omega_b . A^{\frac{1}{k}}} \right)^k \tag{18}$$

with k the order of the filter, M and A are the high and low frequency gains of the filter respectively and ω_b the bandwidth. Design specifications are the same for pitch and yaw rate and, as lateral dynamics are quasi-symmetrical, the weighting filter matrix chosen for the tuning are all scalars. For good tracking and disturbance rejection, $W_s(s)$ was chosen large inside the controller bandwidth resulting in S being attenuated in low frequency. No reference model was used to impose the transient response, however the sensitivity function bandwidth was limited in order to obtain a 2% settling time of 0.35s and 0% overshoot. $W_{KS}(s)$ was designed to limit the controller bandwidth and therefore attenuate its activity in high frequency. In the end, the constraint on sensitivity function was prioritised in the trade-off between good tracking and reduced controller activity because the output of the controller is fed to INDI inner loop before reaching actuators which reduce the control signal amplitude. Nonetheless, a second order high pass filter was used for W_{KS}. In the end, the $\mathscr{H}_\infty$ optimisation problem which needs to be solved can be written as follows:

Over the set of all stabilizing controller K minimises γ as:

$$\left\| \begin{bmatrix} W_S(s)S(s) \\ W_{KS}(s)KS(s) \end{bmatrix} \right\|_\infty < \gamma \tag{19}$$

3.4.4 Design Results

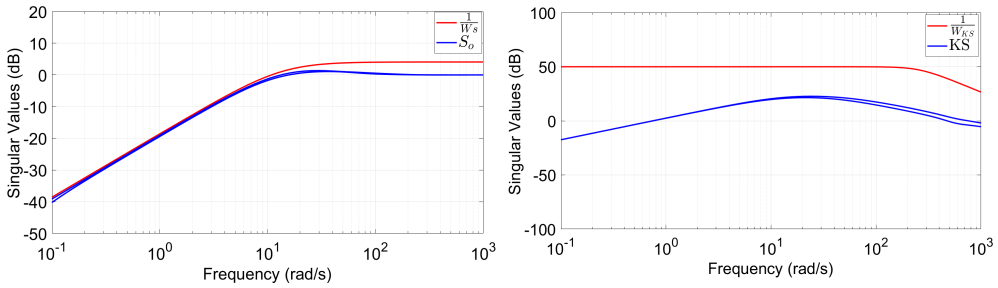

Fig. 6 Lateral channels mixed-sensitivity design results

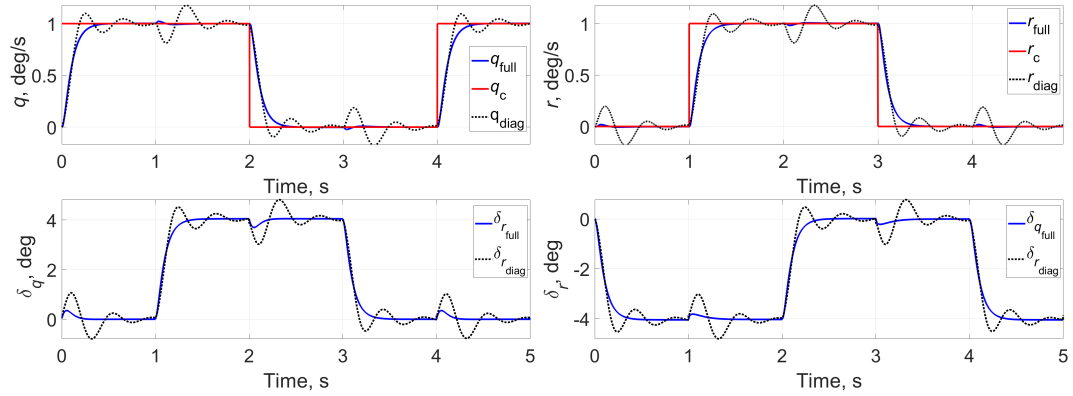

Fig. 7 Lateral channels INDI autopilot results

Figure 7 shows a performance comparison between two INDI autopilots with the same inner loop but with different external controllers tuned with the same design specifications. The first one is a fixed-structured decentralised controller and the other is the proposed tuned full order controller. The simulation was conducted with a nonlinear model of the projectile lateral dynamics for an arbitrary flight point where the parameter vector $\sigma = [V \quad h \quad \alpha \quad \beta \quad p_1]^T$ is constant. The full order controller presents satisfactory reference tracking and decoupling capacity while the decentralised controller is subject to overshoot and oscillations.

3.5 Pitch and Yaw Angles Control

For the control of pitch and yaw angles, a unique linear controller is designed and cascaded with the INDI lateral rate autopilot presented in Section 3.4. No dynamic inversion is needed because the control of lateral dynamics is already guaranteed for all flight envelope. The controller will compute the desired rate q_c, r_c from the desired angles θ_c, ψ_c. The structure of the autopilot is shown in Fig. 8.

3.5.1 Controller Tuning

The design model used for the angle controller is made considering two assumptions. First, looking at the performance of the INDI autopilot for lateral channels decoupling, closed-loop lateral rate dynamics are considered fully decoupled and can be approximated by a first order transfer function:

$$\begin{bmatrix} q \\ r \end{bmatrix} = \begin{bmatrix} \frac{1}{\tau s+1} & 0 \\ 0 & \frac{1}{\tau s+1} \end{bmatrix} \begin{bmatrix} q_c \\ r_c \end{bmatrix} \tag{20}$$

with $\tau = 0.09$ corresponding to a $t_s = 0.35$s. The second assumption made for the design is related to kinematics equations:

$$\begin{cases} \dot{\theta} = q \\ \dot{\psi} = \frac{1}{\cos\theta} r \end{cases} \tag{21}$$

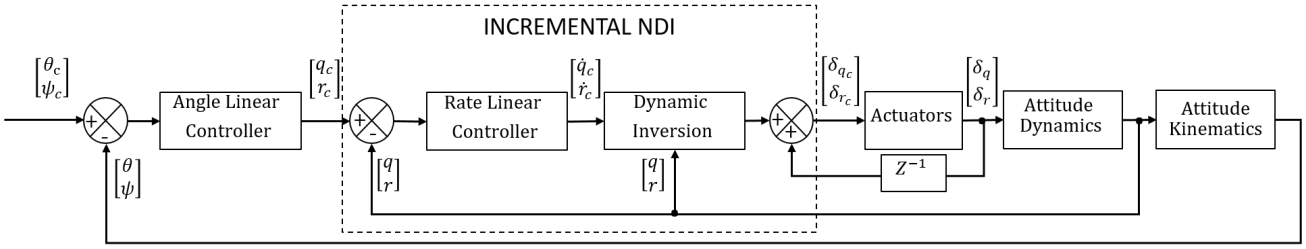

Fig. 8 Attitude autopilot architecture

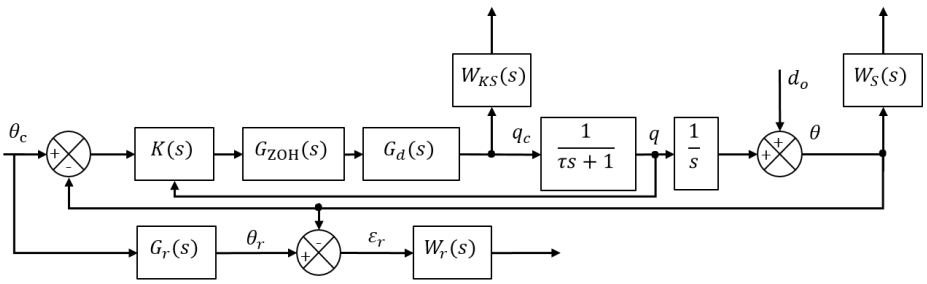

Fig. 9 Pitch controller design layout

The coupling term present in the $\dot{\psi}$ equation is canceled online by multiplying r_c by $\cos\theta$ and therefore, not taken into account in the design model given in Fig. 9. These two assumptions allows us to reduce the design problem to a SISO system as the θ and ψ dynamics are considered fully decoupled and symmetrical. Thus, the controller was tuned for the control of θ and was reused for the control of ψ and a more simple and fixed-structure controller was used for the design. The architecture of the linear controller $K(s)$ is shown in Fig. 10. It consists of a 5 gains controller with a feedforward, servo and regulator parts.

Following the same procedure as for Section 3.4.3, a mixed-sensitivity approach was used but with additional constraints on a second order reference model following. A value of $\omega_r = 5.13$ rad/s and $\xi_r = 0.7797$ was chosen, corresponding to an maximal overshoot of 2% and a settling time of 1 sec.

$$G_r(s) = \frac{\omega_r^2}{s^2 + 2\xi_r\omega_r + \omega_r^2} \tag{22}$$

A first order low pass weighting filter $W_r(s)$ was used to adjust the constraint on the transfer function between θ_c and ε_r on the frequency domain, since a low model matching error is reachable in low frequency but cannot be achieved for an infinite bandwidth. A second order low pass filter $W_S(s)$ was used to guarantee disturbance rejection and a first order high pass filter for $W_{KS}(s)$. Limiting the activity of the controller in high frequency is necessary to avoid fast changing lateral rate q and r. Finally, additional constraints concerning minimal gain and phase margins evaluated at the plant output were imposed. Constraints on model matching error, controller bandwidth and output sensitivity are defined as hard goals for the design and constraints on minimal gain and phase margins are defined as soft goals. The $\mathscr{H}_\infty$ problem which needs to be solved is described as follows:

Minimise K subject to:

$$\left\| W_r(s) T_{\theta_c \to \varepsilon_r(s,K)} \right\|_\infty \leq 1 \tag{23a}$$

$$\left\| W_{S_o}(s) T_{d_o \to \theta(s,K)} \right\|_\infty \leq 1 \tag{23b}$$

$$\left\| W_{KS}(s) T_{\theta_c \to q_c(s,K)} \right\|_\infty \leq 1 \tag{23c}$$

$$GM > 7\text{dB}, PM > 35\text{deg} \tag{23d}$$

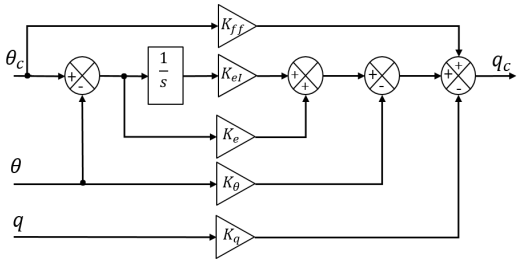

Fig. 10 Pitch controller design layout

3.5.2 Design Results

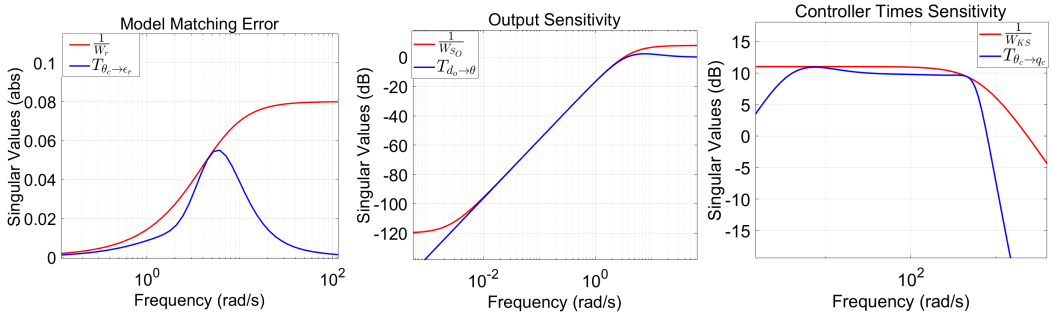

Fig. 11 Pitch controller mixed-sensitivity design results

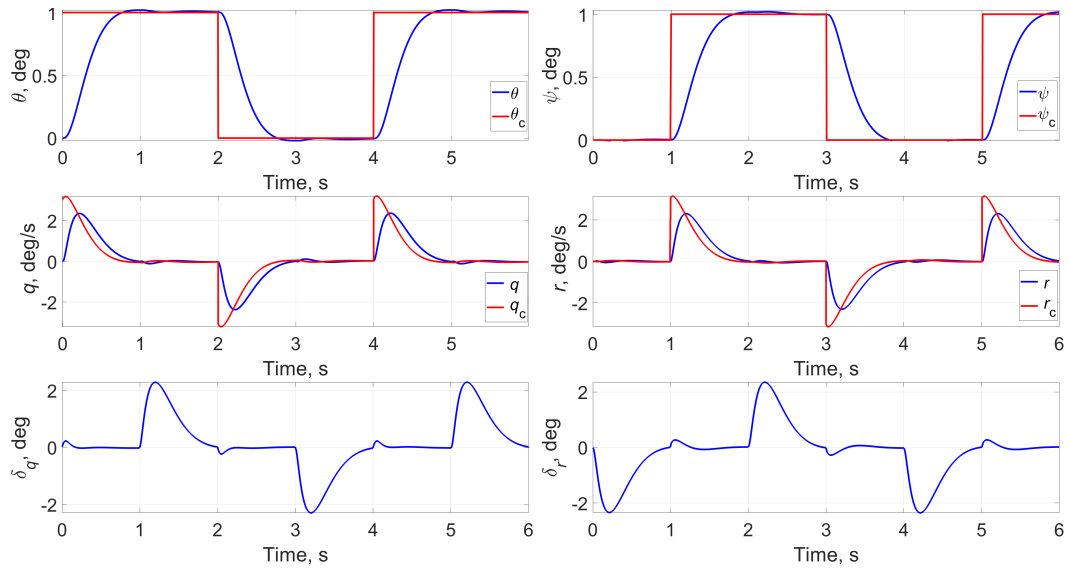

Fig. 12 Pitch/yaw angles INDI autopilot results

The gains were tuned with MATLAB `systune` which uses nonsmooth optimization algorithms [22]. Fig. 11 shows the frequency results for the synthesized controller, all design requirements were met obtaining a low reference model matching error as well as limitation on control usage and well constrained sensitivity function in low frequency. An output gain margin of 32.4 dB is obtained with a phase margin of 53.3 deg corresponding to a delay margin of 0.21 sec. One flight point nonlinear simulation on Fig. 12 confirms the satisfactory design where fully decoupled lateral angles control is achieved.

4 Nonlinear Trajectory Simulations

The last part of this paper is dedicated to full trajectory nonlinear simulation results. Fig. 7 and Fig. 12 showed the lateral rate decoupling and pitch and yaw control for a one flight point nonlinear model, full trajectory simulation are now given with control of the projectile angles. Two simulations are proposed, Fig. 13 shows a top attack scenario where the pitch angle is increased during the last 7 seconds of the trajectory reaching $\theta = 70$ deg at arrival which corresponds to a 40 deg increase compared to ballistic trajectory. Another use case of the proposed autopilot is illustrated by Fig. 14 where the flight paths angles γ and χ are used as reference for θ and ψ respectively in order to reduce the aerodynamic angles α and β resulting in reduced projectile oscillation and increased stability. Even if good reference tracking is achieved in both simulations, limitations of the proposed autopilot are clearly noticeable, the control effort is way above the actuators limitations which are set to 10 deg. However this practical

consideration doesn't necessarily question the relevance of the methodology and the approach proposed in this paper. Several possibilities like anti-windup techniques and low-pass filtered reference angles could be investigated to reduce the amplitude of the control signal and deal with actuators saturation.

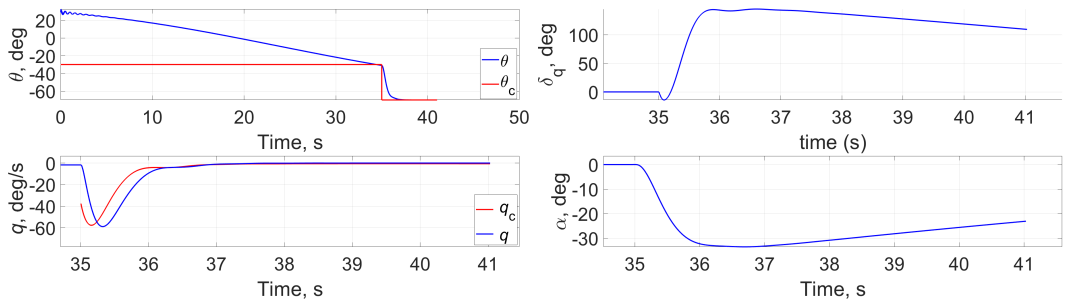

Fig. 13 Nonlinear simulation of a top attack scenario

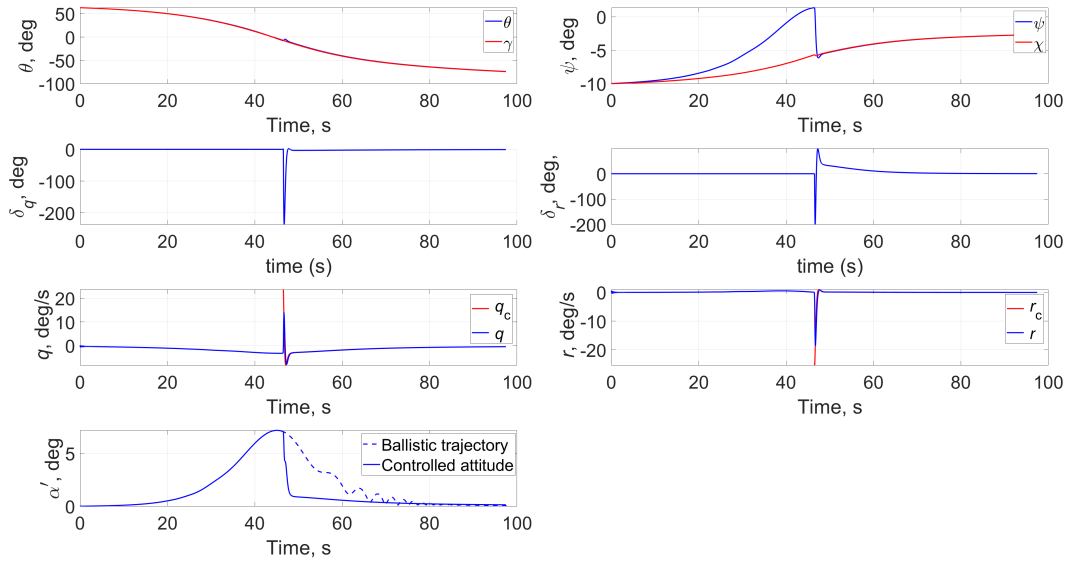

Fig. 14 Nonlinear simulation of a flight path angle autopilot

5 Conclusion

This paper proposes a practical and straightforward design methodology and shows results concerning a novel nonlinear angle autopilot using Incremental Nonlinear Dynamic Inversion applied to the problem of attitude control for a dual-spin 155 mm guided ammunition. Full order $\mathscr{H}_\infty$ controller associated with discrete-time INDI achieved close to perfect decoupling between lateral channels and permits the control of pitch and yaw angles for all flight envelope with a unique cascaded fixed-structure linear controller. The sampling frequency impact on INDI inversion was highlighted and was taken into account during the design. Finally, even if nonlinear simulations demonstrated the relevance of the design approach, further investigations needs to be conducted concerning analytical proof of the inverted model and for actuators saturation.

Appendix

INDI theory :

The continuous-time equations of INDI starts from the general case of a nonlinear system, where $\dot{\boldsymbol{x}}$ is the time derivative of the state vector $\boldsymbol{x}$ and $\boldsymbol{u}$ the control signal vector.

$$\dot{\boldsymbol{x}} = f(\boldsymbol{x}, \boldsymbol{u}) \tag{24}$$

By estimating $\dot{\boldsymbol{x}}$ using a first order Taylor-series approximation, the following expression is obtained:

$$\dot{\boldsymbol{x}} \approx f(\boldsymbol{x}_0, \boldsymbol{u}_0) + \frac{\mathrm{d}f(\boldsymbol{x}, \boldsymbol{u})}{\mathrm{d}\boldsymbol{x}}\Big|_{\boldsymbol{x}=\boldsymbol{x}_0, \boldsymbol{u}=\boldsymbol{u}_0} (\boldsymbol{x} - \boldsymbol{x}_0) + \frac{\mathrm{d}f(\boldsymbol{x}, \boldsymbol{u})}{\mathrm{d}\boldsymbol{u}}\Big|_{\boldsymbol{x}=\boldsymbol{x}_0, \boldsymbol{u}=\boldsymbol{u}_0} (\boldsymbol{u} - \boldsymbol{u}_0) \tag{25}$$

where $\boldsymbol{x}_0$ and $\boldsymbol{u}_0$ are the last available state and control values. To simplify the notation $F\Delta\boldsymbol{x}$ and $G\Delta\boldsymbol{u}$ are defined according to Eq. (26).

$$F\Delta\boldsymbol{x} = \frac{\mathrm{d}f(\boldsymbol{x}, \boldsymbol{u})}{\mathrm{d}\boldsymbol{x}}\Big|_{\boldsymbol{x}=\boldsymbol{x}_0, \boldsymbol{u}=\boldsymbol{u}_0} (\boldsymbol{x} - \boldsymbol{x}_0) \tag{26a}$$

$$G\Delta\boldsymbol{u} = \frac{\mathrm{d}f(\boldsymbol{x}, \boldsymbol{u})}{\mathrm{d}\boldsymbol{u}}\Big|_{\boldsymbol{x}=\boldsymbol{x}_0, \boldsymbol{u}=\boldsymbol{u}_0} (\boldsymbol{u} - \boldsymbol{u}_0) \tag{26b}$$

Combining Eq. (25) and Eq. (26), the following expression is obtained:

$$\dot{\boldsymbol{x}} = \dot{\boldsymbol{x}}_0 + F\Delta\boldsymbol{x} + G\Delta\boldsymbol{u} \tag{27}$$

where G is called the control effectiveness matrix as it is directly related to control input. At this point, the pseudo control variable $\boldsymbol{v}$ is introduced to impose the behaviour of the dynamics as:

$$\dot{\boldsymbol{x}} = \boldsymbol{v} \tag{28}$$

Actuator dynamics are assumed to vary much faster than the state dynamics $\Delta\boldsymbol{x} \ll \Delta\boldsymbol{u}$ so by time scale separation $F\Delta\boldsymbol{x}$ can be neglected. With this assumption, all model parameters related to state dynamics will not be used to computed the control law, reducing drastically the model dependency of the INDI control signal:

$$\dot{\boldsymbol{x}} = \dot{\boldsymbol{x}}_0 + G\Delta\boldsymbol{u} = \boldsymbol{v} \tag{29}$$

Equation (29) leads to the incremental command to compute, assuming that G is invertible :

$$\Delta\boldsymbol{u} = G^{-1}(\boldsymbol{v} - \dot{\boldsymbol{x}}_0) \tag{30}$$

by replacing $\Delta\boldsymbol{u}$ in Eq. (29) by the expression in Eq. (30), the dynamics act like a simple integrator, in the general case the linearized dynamics act as a chain of integrator of the same order as the system. From $\Delta\boldsymbol{u}$ the command $\boldsymbol{u}$ needs to be computed by adding $\Delta\boldsymbol{u}$ to the previous available command.

$$\Delta\boldsymbol{u} = \boldsymbol{u} - \boldsymbol{u}_0 \tag{31a}$$

$$\boldsymbol{u} = \Delta\boldsymbol{u} + \boldsymbol{u}_0 = \boldsymbol{u}_0 + G^{-1}(\boldsymbol{v} - \dot{\boldsymbol{x}}_0) \tag{31b}$$

A discrete-time implementation of INDI is proposed in Ref. [23] and was used in this article. Eq. (32-36) detail the discrete-time reformulation. The future state vector is noted $\boldsymbol{x}_{k+1}$, $\boldsymbol{x}_k$ and $\boldsymbol{u}_k$ are the current state and actuator measurement vector respectively, and T is the sampling period.

$$\begin{aligned} \boldsymbol{x}_{k+1} &= \boldsymbol{x}_k + \int_{t_k}^{t_{k+1}} f(\boldsymbol{x}_k, \boldsymbol{u}_k), \mathrm{d}t \\ &= \boldsymbol{x}_k + T f(\boldsymbol{x}_k, \boldsymbol{u}_k) \end{aligned} \tag{32}$$

The future state derivative $\dot{\boldsymbol{x}}_{k+1}$ can be estimated by using Euler forward method.

$$\frac{\boldsymbol{x}_{k+1}-\boldsymbol{x}_k}{T} = f(\boldsymbol{x}_k,\boldsymbol{u}_k) \approx \dot{\boldsymbol{x}}_{k+1} \tag{33}$$

The discrete-time equivalent of Eq. (27) is given by :

$$\dot{\boldsymbol{x}}_{k+1} \approx f(\boldsymbol{x}_k,\boldsymbol{u}_k) + F(\boldsymbol{x}_k,\boldsymbol{u}_k)(\boldsymbol{x}_{k+1}-\boldsymbol{x}_k) + G(\boldsymbol{x}_k,\boldsymbol{u}_k)(\boldsymbol{u}_{k+1}-\boldsymbol{u}_k) \tag{34}$$

however the future state $\boldsymbol{x}_{k+1}$ and control value $\boldsymbol{u}_{k+1}$ are not known at instant k so Eq. (34) is reformulated to be implementable:

$$\dot{\boldsymbol{x}}_k \approx \frac{\boldsymbol{x}[k]-\boldsymbol{x}[k-1]}{T} + G(\boldsymbol{x}_{k-1},\boldsymbol{u}_{k-1})(\boldsymbol{u}_k-\boldsymbol{u}_{k-1}) = \boldsymbol{v}_{k-1} \tag{35}$$

The next command that will linearize the system dynamics can be computed from current and previous state and current control signal. The pseudo control variable $\boldsymbol{v}[k]$ is determined by the outer loop linear controller:

$$\boldsymbol{u}[k+1] = \boldsymbol{u}[k] + G^{-1}\left(\boldsymbol{v}[k] - \frac{\boldsymbol{x}[k]-\boldsymbol{x}[k-1]}{T}\right) \tag{36}$$

Modified Continuous Design :

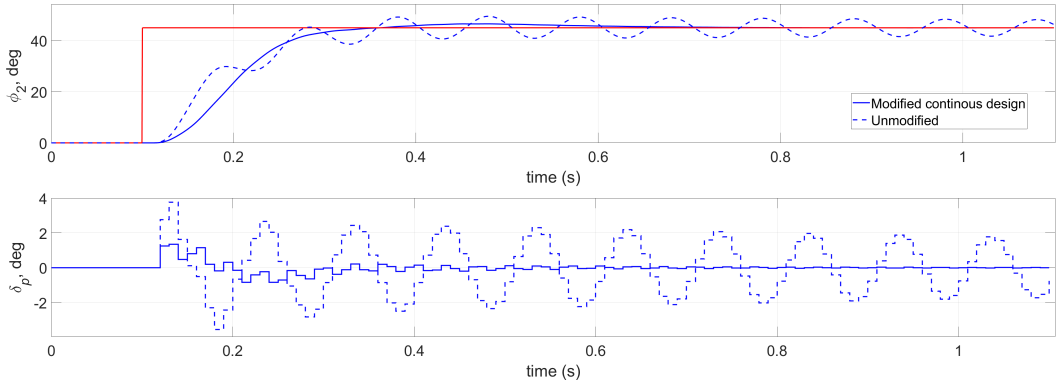

Fig. 15 Response of digital controller using modified and unmodified continuous-time design

Lateral channel decoupling mixed-sensitivity design:

$$W_S(s) = \begin{bmatrix} \frac{\frac{s}{1.6}+8.5}{s+8.5.10^{-4}} & 0 \\ 0 & \frac{\frac{s}{1.6}+8.5}{s+8.5.10^{-4}} \end{bmatrix} \tag{37}$$

$$W_{KS}(s) = \begin{bmatrix} \left(\frac{\frac{s}{\sqrt{5.55}}+250}{s+250.\sqrt{315}}\right)^2 & 0 \\ 0 & \left(\frac{\frac{s}{\sqrt{5.55}}+250}{s+250.\sqrt{315}}\right)^2 \end{bmatrix} \tag{38}$$

Pitch and yaw angles controller design:

$$W_r(s) = \frac{\frac{s}{0.08}+60}{s+60.10^{-4}} \tag{39}$$

$$W_S(s) = \frac{\frac{s}{\sqrt{2.5}} + 2.5}{s + 2.53.\sqrt{10^{-6}}} \tag{40}$$

$$W_{KS}(s) = \frac{\frac{s}{0.03} + 2.10^4}{s + 2.10^4.3.55} \tag{41}$$

References

[1] Florian Seve, Spilios Theodoulis, Philippe Wernert, Michel Zasadzinski, and Mohamed Boutayeb. Gain-scheduled $\mathscr{H}_\infty$ loop-shaping autopilot design for spin-stabilized canard-guided projectiles. *AerospaceLab Journal*, 13, December 2017. DOI: 10.12762/2017.AL13-03.

[2] Spilios Theodoulis, Florian Sève, and Philippe Wernert. Robust gain-scheduled autopilot design for spin-stabilized projectiles with a course-correction fuze. *Aerospace Science and Technology*, 42, April 2015. DOI: 10.1016/j.ast.2014.12.027.

[3] Sovanna Thai, Spilios Theodoulis, Clément Roos, and Jean-Marc Biannic. Robust design for the roll-channel autopilot of a canard-guided dual-spin projectile. *IFAC-PapersOnLine, 2019, 21st IFAC Symposium on Automatic Control in Aerospace ACA*, 52(12), January 2019. DOI: 10.1016/j.ifacol.2019.11.248.

[4] Spilios Theodoulis, Vincent Gassmann, Philippe Wernert, Leonidas Dritsas, Ioannis Kitsios, and Anthony Tzes. Guidance and control design for a class of spin-stabilized fin-controlled projectiles. *Journal of Guidance, Control, and Dynamics*, 36(2), March 2013. DOI: 10.2514/1.56520.

[5] D. J. Leith and W. E. Leithead. Survey of gain-scheduling analysis and design. *International Journal of Control*, 73(11), January 2000. DOI: 10.1080/002071700411304.

[6] J. Karl Hedrick and Swaminathan Gopalswamy. Nonlinear flight control design via sliding methods. *Journal of Guidance, Control, and Dynamics*, 13(5), September 1990. DOI: 10.2514/3.25411.

[7] Yuanchuan Shen, Jianqiao Yu, Guanchen Luo, Xiaolin Ai, Zhenyue Jia, and Fangzheng Chen. Observer-based adaptive sliding mode backstepping output-feedback DSC for spin-stabilized canard-controlled projectiles. *Chinese Journal of Aeronautics*, 30(3), June 2017. DOI: 10.1016/j.cja.2017.01.004.

[8] Giovanni Mattei and Salvatore Monaco. Nonlinear autopilot design for an asymmetric missile using robust backstepping control. *Journal of Guidance, Control, and Dynamics*, 37(5), September 2014. DOI: 10.2514/1.g000434.

[9] R. R. da Costa, Q. P. Chu, and J. A. Mulder. Reentry Flight Controller Design Using Nonlinear Dynamic Inversion. *Journal of Spacecraft and Rockets*, 40(1), January 2003. DOI: 10.2514/2.3916.

[10] Jacob Reiner, Gary J. Balas, and William L. Garrard. Robust dynamic inversion for control of highly maneuverable aircraft. *Journal of Guidance, Control, and Dynamics*, 18(1), January 1995. DOI: 10.2514/3.56651.

[11] Steven Tipàn, Spilios Theodoulis, Sovanna Thai, and Michael Proff. Nonlinear Dynamic Inversion Flight Control Design for Guided Projectiles. *Journal of Guidance, Control, and Dynamics*, 43(5), May 2020. DOI: 10.2514/1.G004976.

[12] S. Antony Snell, Dale F. Enns, and William L. Garrard. Nonlinear inversion flight control for a supermaneuverable aircraft. *Journal of Guidance, Control, and Dynamics*, 15(4), July 1992. DOI: 10.2514/3.20932.

[13] Xuerui Wang, Erik-Jan van Kampen, Qiping Chu, and Peng Lu. Stability Analysis for Incremental Nonlinear Dynamic Inversion Control. *Journal of Guidance, Control, and Dynamics*, 42(5), May 2019. DOI: 10.2514/1.G003791.

[14] S. Sieberling, Q. P. Chu, and J. A. Mulder. Robust Flight Control Using Incremental Nonlinear Dynamic Inversion and Angular Acceleration Prediction. *Journal of Guidance, Control, and Dynamics*, 33(6), November 2010. DOI: 10.2514/1.49978.

[15] Paul Acquatella B., Wim van Ekeren, and Qi Ping Chu. PI(D) tuning for Flight Control Systems via Incremental Nonlinear Dynamic Inversion. *IFAC-PapersOnLine*, 50(1), July 2017. DOI: 10.1016/j.ifacol.2017.08.1265.

[16] Ewoud J. J. Smeur, Qiping Chu, and Guido C. H. E. de Croon. Adaptive incremental nonlinear dynamic inversion for attitude control of micro air vehicles. *Journal of Guidance, Control, and Dynamics*, 39(3):450–461, March 2016. DOI: 10.2514/1.g001490.

[17] Sigurd Skogestad and Ian Postlethwaite. *Multivariable Feedback Control: Analysis and Design*. Wiley-Interscience, paperback edition, 11 2005.

[18] Peter H. Zipfel. *Modeling and Simulation of Aerospace Vehicle Dynamics, Third Edition*. American Institute of Aeronautics and Astronautics, Inc., February 2014. DOI: 10.2514/4.102509.

[19] P. Smith. A simplified approach to nonlinear dynamic inversion based flight control. In *23rd Atmospheric Flight Mechanics Conference*, August 1998. DOI: 10.2514/6.1998-4461.

[20] B.J. Bacon, A.J. Ostroff, and S.M. Joshi. Reconfigurable NDI controller using inertial sensor failure detection & isolation. *IEEE Transactions on Aerospace and Electronic Systems*, 37(4), 2001. DOI: 10.1109/7.976972.

[21] Brian L. Stevens, Frank L. Lewis, and Eric N. Johnson. *Aircraft Control and Simulation: Dynamics, Controls Design, and Autonomous Systems*. John Wiley & Sons, Inc, November 2015. DOI: 10.1002/9781119174882.

[22] Pierre Apkarian and Dominikus Noll. Controller design via nonsmooth multidirectional search. *SIAM Journal on Control and Optimization*, 44(6), January 2006. DOI: 10.1137/s0363012904441684.

[23] Ronald van 't Veld, Erik-Jan Van Kampen, and Q Ping Chu. Stability and robustness analysis and improvements for incremental nonlinear dynamic inversion control. In *AIAA Guidance, Navigation, and Control Conference*, January 2018. DOI: 10.2514/6.2018-1127.